

# Supercells and Tornado-like Vortices in an Idealized Global Atmosphere Model

Kai-Yuan Cheng<sup>1</sup>, Shian-jiann Lin<sup>2</sup>, Lucas Harris<sup>3</sup>, and Linjiong Zhou<sup>4</sup>

<sup>1</sup>Princeton University

<sup>2</sup>Affiliation not available

<sup>3</sup>GFDL

<sup>4</sup>Cooperative Institute for Modeling Earth Systems, and Program on Atmospheric and Oceanic Sciences, Princeton University

November 8, 2023

## Abstract

We investigate the representation of individual supercells and intriguing tornado-like vortices in a simplified, locally-refined global atmosphere model. The model, featuring grid stretching, can locally enhance the model resolution and economically reach the cloud-resolving scale. Given an unstable sheared environment, the model can simulate supercells realistically, with a near-ground vortex and funnel cloud at the center of a rotating updraft reminiscent of a tornado. An analysis of the vorticity budget suggests that the updraft core of the supercell tilts environmental horizontal vorticity into the tornado-like vortex. The updraft also acts to amplify the vortex through vertical stretching. Results suggest that the simulated vortex is dynamically similar to observed tornadoes and modeling studies at much higher horizontal resolution.

1                    **Supercells and Tornado-like Vortices in an Idealized Global Atmosphere Model**

2   **Kai-Yuan Cheng<sup>1,2</sup>, Shian-Jiann Lin<sup>3</sup>, Lucas Harris<sup>2</sup>, and Linjiong Zhou<sup>1,2</sup>**

3   <sup>1</sup>Program in Oceanic and Atmospheric Sciences, Princeton University, Princeton, NJ, USA.

4   <sup>2</sup>NOAA/Geophysical Fluid Dynamics Laboratory, Princeton, NJ, USA.

5   <sup>3</sup>Tianji Meteorological Sciences and Technology Inc., Beijing, China.

6  
7   Corresponding author: Kai-Yuan Cheng ([kai-yuan.cheng@noaa.gov](mailto:kai-yuan.cheng@noaa.gov))

8   **Key Points:**

- 9        • A stretched-grid global model can realistically simulate individual supercells and cloudy  
10        tornado-like vortices at kilometer scales
- 11        • The vortex is initiated and maintained by the updraft core by tilting the near-ground  
12        environmental horizontal vorticity vertically
- 13        • The dynamics of the vortices is consistent with previous studies on tornadogenesis  
14

## 15 **Abstract**

16 We investigate the representation of individual supercells and intriguing tornado-like vortices in  
17 a simplified, locally-refined global atmosphere model. The model, featuring grid stretching, can  
18 locally enhance the model resolution and economically reach the cloud-resolving scale. Given an  
19 unstable sheared environment, the model can simulate supercells realistically, with a near-ground  
20 vortex and funnel cloud at the center of a rotating updraft reminiscent of a tornado. An analysis  
21 of the vorticity budget suggests that the updraft core of the supercell tilts environmental  
22 horizontal vorticity into the tornado-like vortex. The updraft also acts to amplify the vortex  
23 through vertical stretching. Results suggest that the simulated vortex is dynamically similar to  
24 observed tornadoes and modeling studies at much higher horizontal resolution.

## 25 **Plain Language Summary**

26 We use a simplified global model to study individual supercells and intriguing cloudy vortices  
27 that behave like tornadoes. This model incorporates grid-stretching techniques, making it a cost-  
28 effective tool to study supercells on a full-size Earth. The model can realistically simulate  
29 supercells and cloudy tornado-like vortices even at kilometer scales, which appears  
30 unprecedented in the literature. We find that the physics behind the vortices is consistent with  
31 previous studies, including observations of tornadogenesis and simulations at much higher  
32 resolution.

## 33 **1 Introduction**

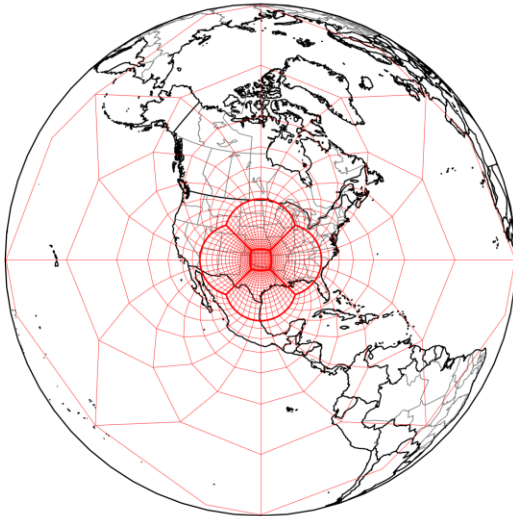
34 A supercell (an intense convective storm characterized by a single quasi-steady rotating  
35 updraft) is often associated with severe weather for its capabilities of producing destructive  
36 winds, large hailstones, extreme precipitation, and dangerous tornadoes. Many field campaigns,  
37 such as RELAMPAGO (Remote sensing of Electrification, Lightning, And  
38 Mesoscale/microscale Processes with Adaptive Ground Observations; Nesbitt et al. 2021) and  
39 VORTEX2 (Verification of the Origins of Rotation in Tornadoes Experiment 2; Wurman et al.,  
40 2012), provide invaluable datasets for understanding the processes associated with supercells.  
41 Those observations, however, are subject to the field of view for a remote sensing device or  
42 sample size for an in-situ instrument. On the other hand, a numerical model can provide a  
43 comprehensive picture of a supercell, i.e., all variables at every grid cell within a computational  
44 domain.

45 Historically, simulations of supercells were feasible only in limited-area domains (e.g.,  
46 Klemp & Wilhelmson, 1978; Schlesinger, 1978; Wang et al., 2016; Orf et al., 2016) due to the  
47 cost of both high temporal and spatial resolutions that are required to resolve supercells. These  
48 limited-area models limit the ability for the simulated storm to interact with its larger-scale  
49 environment. Nowadays, because of continuous advances in computational capacity, the  
50 atmospheric sciences community is ushering in a new era of global cloud-resolving models.

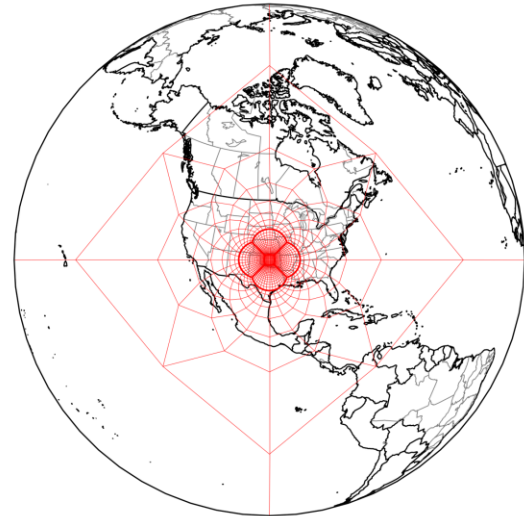
51 Several numerical modeling centers are working on the development of global cloud-resolving  
 52 models with 2-5 km horizontal resolution that can explicitly resolve deep convection (Satoh et  
 53 al., 2019; Stevens et al., 2019; Cheng et al. 2022). The ability of a global model to represent deep  
 54 convection not only reduces the uncertainty caused by cumulus parameterizations (e.g., Stevens  
 55 & Bony, 2013), but it also paves the way toward a better understanding of multiscale interaction  
 56 involving convection (e.g., Madden-Julian Oscillation and cloud feedback; Zavadoff et al. 2023).  
 57 While this new class of global models has been proven useful for understanding the properties of  
 58 intense convection on a global scale (Cheng et al., 2022; Harris et al., 2023), these models are at  
 59 best marginally able to accurately simulate individual supercells. In fact, this group of global  
 60 models is referred to as global storm-resolving models in numerous studies (e.g., Judt et al.,  
 61 2021; Nugent et al., 2022).

62

(a) r20



(b) r40



63

64 **Figure 1.** Illustration of two stretched grid configurations for a C512 cubed-sphere grid. Grids  
 65 are shown by light red lines and the cubed-sphere edges are shown by heavy red lines. Each grid  
 66 box represents 64 by 64 actual grid cells. (a) r20 configuration, the finest grid spacing is about 1  
 67 km; (b) r40, ~500 m. Borders, countries, and states are plotted as a reference scale for  
 68 demonstration purposes.

69

70 In this study, we describe an efficient nonhydrostatic global model using grid stretching,  
 71 and conduct idealized simulations of a supercell at various resolutions on cloud-resolving scales,  
 72 ranging from 4 km down to 500 m. The configuration of the simulation is similar to the supercell

73 test case used in the 2016 Dynamical Core Model Intercomparison Project (DCMIP2016; Ullrich  
74 et al., 2017; Zarzycki et al., 2019). Unlike the DCMIP2016 simulations that were conducted on a  
75 small Earth with its radius reduced by a factor of 120, our simulations are conducted on a full-  
76 size Earth. Figure 1 shows examples of the grid configurations used in this study. Our model  
77 features grid-stretching, which can reach cloud-resolving scales while requiring less than one  
78 one-thousandth of the computational resources that would be needed for the simulation to be  
79 performed at the same resolution globally. Our model can realistically simulate individual  
80 supercells and even intriguing vortices that develop near the ground and are qualitatively similar  
81 to tornadoes. We refer to those vortices as “tornado-like vortices”, analogous to the so-called  
82 “tropical cyclone-like vortices” in 20-100 km global models (e.g., Zhao et al., 2012). We believe  
83 that this is the first time such vortices have ever been simulated in a full-size Earth global model.

## 84 **2 Model Description and Simulation Design**

85 An idealized nonhydrostatic global model that can reach the cloud-resolving scale locally  
86 is developed for this study. The model is powered by the finite-volume cubed-sphere dynamical  
87 core (FV3) developed at the Geophysical Fluid Dynamics Laboratory (GFDL). The dynamical  
88 core solves the vector-invariant Euler equations for atmospheric motions using the C-D grid  
89 algorithm of Lin & Rood (1997) on a gnomonic cubed-sphere (Putman & Lin, 2007) and a  
90 Lagrangian vertical coordinate (Lin, 2004). The pressure gradient force is solved by the finite-  
91 volume algorithm of Lin (1997). The nonhydrostatic component is handled by a vertically semi-  
92 implicit scheme described in Harris et al. (2020). For physics parameterization, we use the  
93 GFDL microphysics scheme, version 3 (Zhou et al., 2022) with warm-rain processes only for  
94 simplicity, which has been previously used in the study of anvil cloud fraction (Jeevanjee and  
95 Zhou, 2022). They found that the warm-rain only and the full microphysics produce similar  
96 cloud structures.

97 FV3 can refine the cubed-sphere by an analytical “stretching” (Schmidt 1977; Harris et  
98 al., 2016), which allows it to enhance the resolution locally down to cloud-resolving scales and  
99 even finer. For this study, four configurations of the cubed-sphere grid are used to achieve  
100 different horizontal resolutions. A cubed-sphere with  $128 \times 128$  (C128) and  $256 \times 256$  (C256)  
101 cells on each face is stretched by a factor of 20 to reach minimum grid-cell widths of 4 and 2 km,  
102 respectively. A cubed-sphere with  $512 \times 512$  (C512) cells on each face is stretched by a factor of  
103 20 and 40 to reach minimum grid-cell widths of 1 km and 500 m, respectively. Figure 1 shows

104 examples of stretched C512 cubed-sphere grids in the 1 km and 500 m cases. The center of the  
 105 high-resolution region is placed at 35.4° N and 262.4° W for demonstration purposes. The  
 106 location of the high-resolution region has no effect on the solution since the Earth's rotation is  
 107 turned off. The grid configurations are summarized in Table 1. All simulations use 90 vertical  
 108 levels with a top at 50 hPa. The vertical layer thickness is finest at the bottom level (~8 m) and  
 109 gradually expands with height.

110

| Resolution (km) | Cubed-sphere resolution | Grid-stretching factor | Acoustic timestep (s) |
|-----------------|-------------------------|------------------------|-----------------------|
| 4               | 128                     | 20                     | 5.0                   |
| 2               | 256                     | 20                     | 2.5                   |
| 1               | 512                     | 20                     | 1.25                  |
| 0.5             | 512                     | 40                     | 0.625                 |

111 **Table 1.** Configuration of grid and timestep for each simulation.

112

113 All simulations are initialized using the environment of Toy (2012) with modifications.  
 114 This environment is favorable for the development of supercells. The thermodynamic profile is  
 115 adapted from Weisman and Klemp (1982). The environment has a convective available potential  
 116 energy of 2515 J·kg<sup>-1</sup>. For the wind profile ( $U$  and  $V$  in a local Cartesian system), an analytic  
 117 approximation of Toy's profile is used:

$$U(z) = 15 \text{ m} \cdot \text{s}^{-1} \left[ 1 + \tanh\left(\frac{z - 3 \text{ km}}{2 \text{ km}}\right) \right] - 8.5 \text{ m} \cdot \text{s}^{-1}$$

$$V(z) = 8.5 \text{ m} \cdot \text{s}^{-1} \left[ \tanh\left(\frac{z}{1 \text{ km}}\right) - 0.5 \right],$$

118  
119 (1)

120 where  $z$  is the altitude in km.

121 The wind profile is then mapped onto a spherical domain ( $u$  and  $v$  in a spherical  
 122 coordinate system) by multiplying a horizontal Gaussian:

$$u(\lambda, \theta, z) = U(z) \exp\left(-\frac{8D}{R_e}\right), \quad (2)$$

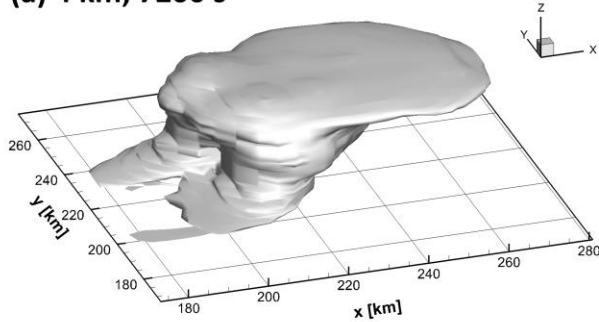
124 and similarly for  $v(\lambda, \theta, z)$ , where  $\lambda$  and  $\theta$  are longitude and latitude, respectively;  $D$  is the great-  
 125 circle distance from the center of the high-resolution region;  $R_e$  is the radius of the Earth.

126 The model uses a warm bubble to initiate convection. For all simulations, the thermal  
 127 perturbation of the warm bubble is 2 K. The radial dimension of the bubble is 10 km in the

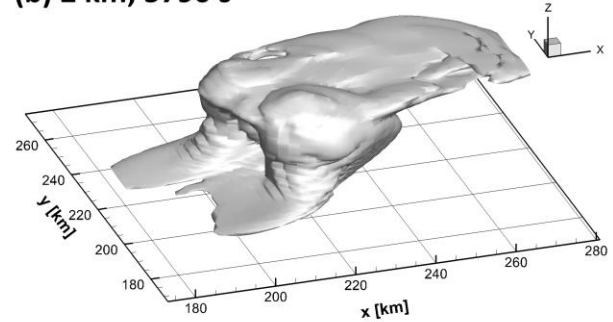
128 horizontal direction and 1.4 km in the vertical direction. All four simulations are integrated for 2  
 129 hours with the same physics timestep of 5 s. The acoustic timestep varies with different  
 130 resolutions and is tabulated in Table 1.

131

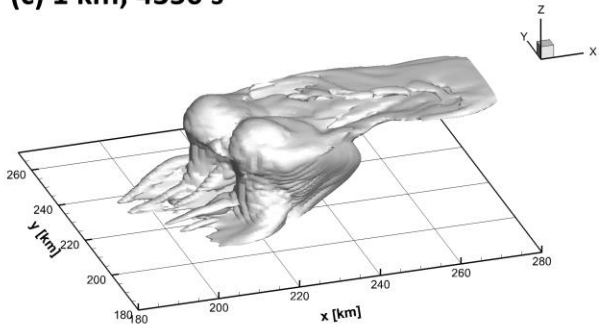
(a) 4 km; 7200 s



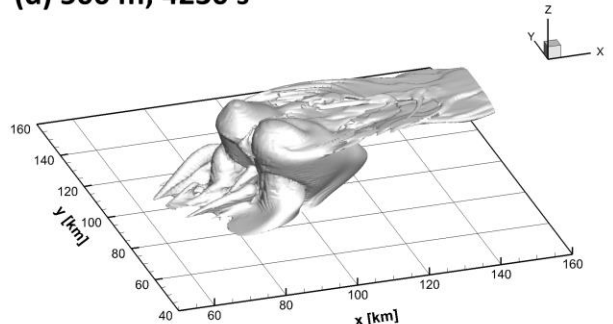
(b) 2 km; 5790 s



(c) 1 km; 4350 s



(d) 500 m; 4230 s



132

133 **Figure 2** Perspective view of a supercell in its mature stage for the (a) 4 km, (b) 2 km, (c) 1 km,  
 134 and (d) 500 m simulations. The white isosurface depicts the appearance of the supercell, which is  
 135 defined by  $0.1 \text{ g}\cdot\text{kg}^{-1}$  in total hydrometeor  $q_l$  (a combination of cloud water  $q_c$  and rainwater  $q_r$ ).  
 136 The simulation time of the snapshot is indicated.

137

### 138 3 Supercell in a Global Model

139 Our global model is capable of simulating an individual supercell realistically at all four  
 140 resolutions considered. Despite having varied horizontal resolutions, all simulated supercells  
 141 show similarities in terms of storm morphology. After initialization, the supercell goes through  
 142 the cumulus stage and persists in the mature stage. Figure 2 shows the appearance of the  
 143 supercell in its mature stage at different resolutions. Common storm features can be seen,  
 144 including protruding overshooting tops and a wide-spreading anvil. All simulations have a storm

145 of similar dimensions: about 40 km in both  $x$  and  $y$  directions. As for the vertical dimension, the  
146 storm in each simulation can grow over the height of 15 km. Such similarity in the dimension is  
147 a result of the same warm bubble used to initialize the simulations. At higher resolutions,  
148 expectedly, the supercell's appearance becomes more complicated, as turbulent motions at small  
149 scales are better resolved. The overshooting top becomes more prominent, and the anvil shows  
150 more wave structures. Also, the supercell at a higher resolution tends to grow faster with more  
151 intense updrafts than that at a lower resolution. Such dependencies on grid spacing are consistent  
152 with previous studies (e.g., Noda & Niino, 2003; Potvin & Flora, 2015).

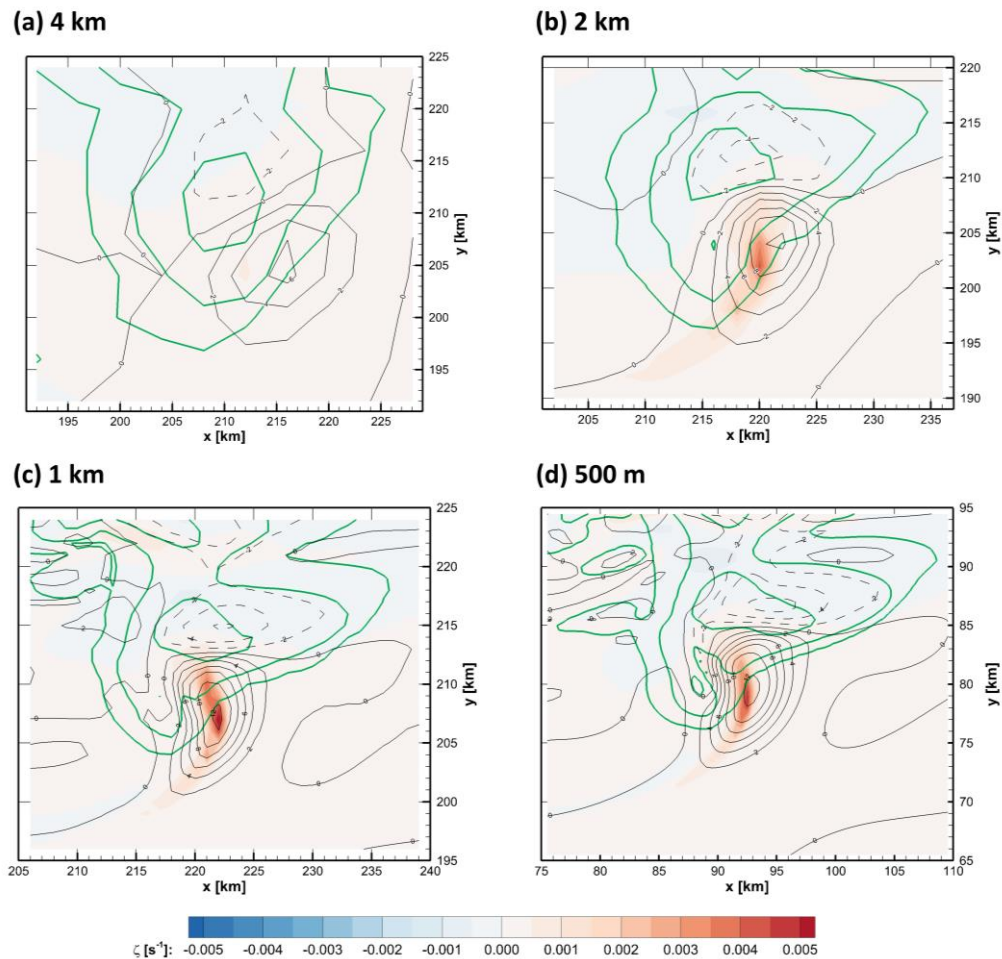
153 It is worth noting that the supercell in all cases is splitting, which is intrinsic storm  
154 dynamics given the vertically veered low-level wind profile. The behavior of storm splitting is  
155 consistent with previous studies using similar wind profiles (e.g., Toy, 2012; Weisman &  
156 Rotunno, 2000). At a higher resolution, the splitting occurs more quickly and prominently. One  
157 possible explanation is that the vortex dynamics and pressure perturbations are better resolved at  
158 a higher resolution, which plays an important role in the storm splitting.

159 Next, we examine the dynamics of the simulated supercell, focusing on the stronger  
160 right-moving (clockwise-rotating) cell. Figure 3 shows the horizontal distribution of vertical  
161 vorticity  $\zeta$ , vertical velocity  $w$ , and  $q_l$  in all simulations.  $\zeta$  and  $q_l$  are from the level near the  
162 ground ( $\sim 27$  m AGL), while  $w$  is from another level aloft ( $\sim 1.74$  km AGL).  $\zeta$  and  $w$  are used to  
163 illustrate the dynamics of the supercell whereas  $q_l$  is used to depict the shape of the supercell.  
164 From  $q_l$  distribution, it can be seen that the supercell in all cases gets twisted by the clockwise  
165 hodograph curvature (Equation 1). At higher resolutions, the bending of the storm becomes more  
166 prominent. All simulations, except for the 4 km case, show a hook-shaped pattern, resembling  
167 the hook echo radar signature of a supercell. In particular, the hook-shaped pattern is well-  
168 resolved in the 1 km and 500 m simulations. A hook echo signature is a useful indication of  
169 tornadogenesis, as discussed by many studies (e.g., Markowski, 2002). Indeed, all simulations,  
170 except for 4 km, have "tornado-like" vortices forming near the ground. We will examine those  
171 vortices in detail and discuss their formation in the following section.

172 In addition to the hook-shaped pattern, common storm structures such as forward flank  
173 downdraft (FFD) and rear flank downdraft (RFD) can be seen in Figure 3, especially in the high-  
174 resolution simulations (1 km and 500 m). Take the 1 km simulation for example (Figure 3c), an  
175 FFD is shown by a region of strong and well-organized downdrafts, primarily generated by

176 precipitation loading and evaporative cooling, north to the main updraft at  $x = 220.0$  km and  $y =$   
 177 216.0 km. An RFD develops west to the main updraft around  $x = 210.0$  km and  $y = 205.0$  km  
 178 (roughly outlined by the zero contour of  $w$ ), a weak and loosely defined downdraft is forced  
 179 primarily by vertical pressure gradient.

180

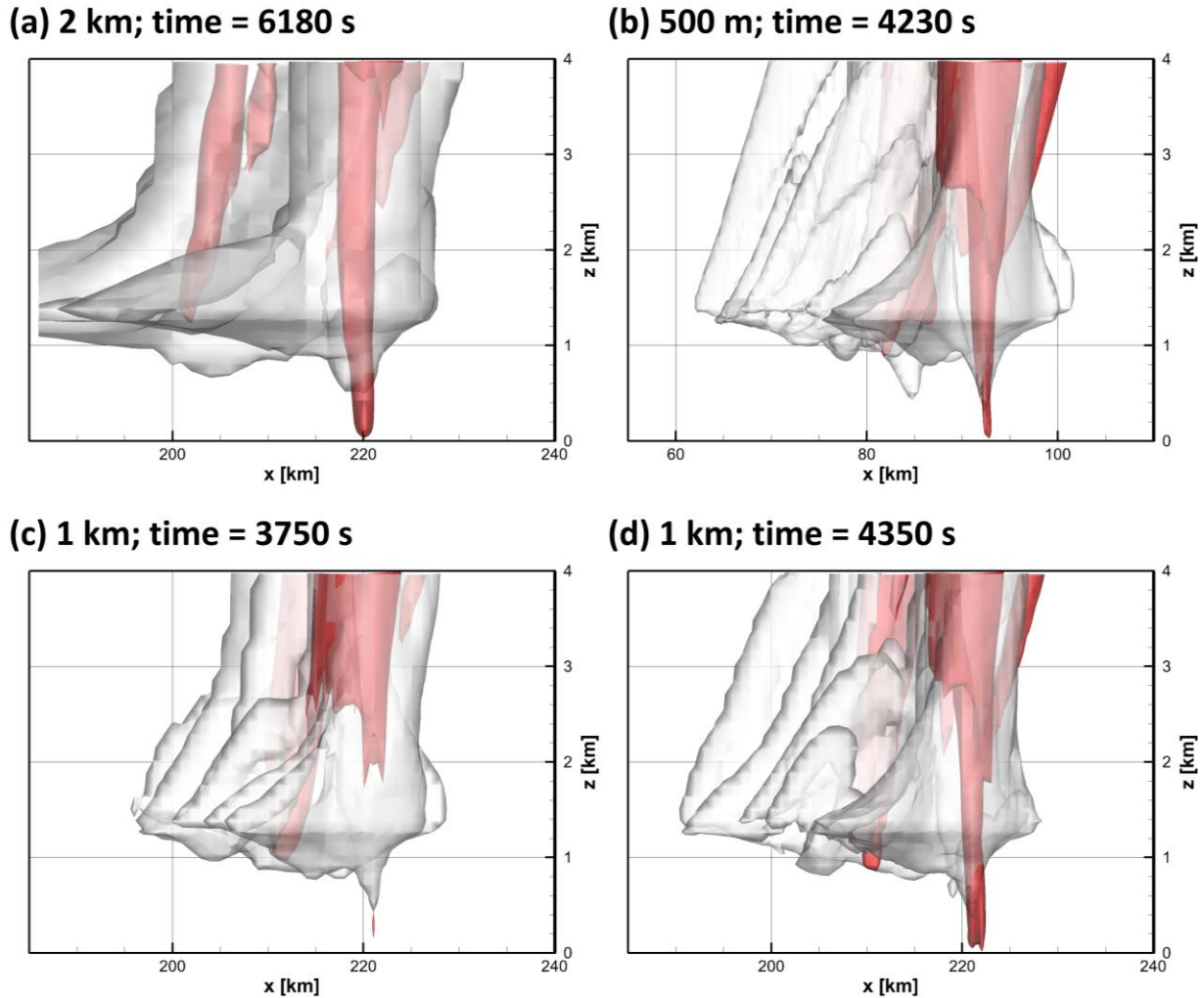


181  
 182 **Figure 3.** Dynamical structure of the clockwise-rotating right-moving cell in the mature stage in  
 183 (a) 4 km, (b) 2 km, (c) 1 km, and (d) 500 m simulations at the same time as in Figure 2. Color  
 184 shading and green contours are  $w$  and  $q_l$ , respectively, near the ground ( $\sim 27$  m AGL). The  $q_l$   
 185 contours are 0.1, 1.0, and  $5.0 \text{ g}\cdot\text{kg}^{-1}$ . Black contours show  $w$  at an AGL of  $\sim 1.74$  km. The  $w$   
 186 contour interval is  $2 \text{ m s}^{-1}$ , with negative contours dashed.

187

188 The storm morphology and the dynamical features are consistent with previous  
 189 observational and theoretical studies (e.g., Figure 2 in Davies-Jones, 2015). In the 4-km

190 simulation, the overshooting top, RFD, and FFD are not as prominent as in other cases at a  
 191 higher resolution. Nevertheless, the dynamics of the supercell in the 4-km simulation are  
 192 qualitatively similar to that in the high-resolution ones. The result indicates that our global model  
 193 is capable of reproducing a supercell storm realistically.  
 194



195  
 196 **Figure 4.** Development of cloudy tornado-like vortex. (a) 6180 s in 2 km, (b) 4230 s in 500 m,  
 197 (c) 3750 s and (d) 4350 s in 1 km simulation. The solid red isosurface is  $\zeta = 0.005 \text{ s}^{-1}$ , while the  
 198 transparent white isosurface is  $q_c = 0.1 \text{ g} \cdot \text{kg}^{-1}$ .

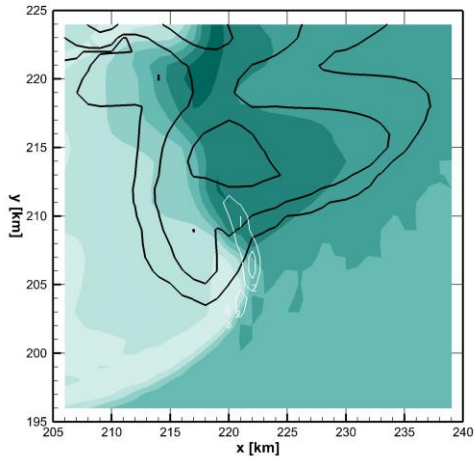
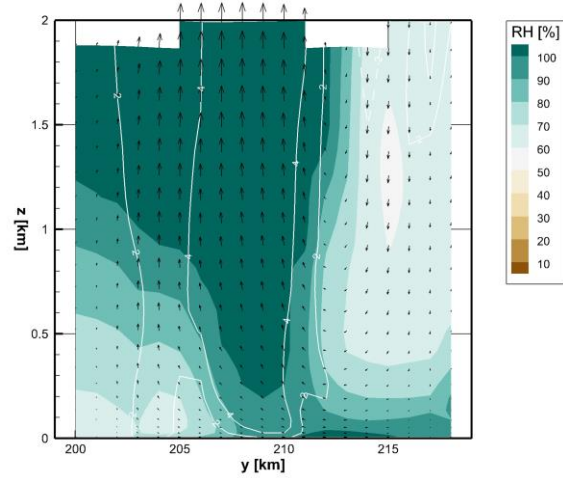
#### 199 **4 Tornado-like Vortex**

200 In this section, we report and discuss the existence of an intriguing cloudy vortex that  
 201 develops near the ground in all cases except for the 4 km (Figures 3 and 4). As the vortices in  
 202 those three simulations are similar physically, we use the 1 km simulation only to illustrate the

203 physics and formation of the vortex. The horizontal distribution of  $\zeta$  near the ground in the 1 km  
204 simulation can be seen in Figure 3c. A strong  $\zeta$  is developing locally at  $x = 222.0$  km and  $y =$   
205  $207.0$  km, near the hook-shaped pattern in  $q_l$  discussed previously. The strong  $\zeta$  is a horizontal  
206 cross-section of a 3-D vortex. Figure 4c and d show the development of the cloudy vortex near  
207 the ground. At 3750 s into the simulation, where the supercell is in its mature stage, a local  $\zeta$  is  
208 developing at  $x = 221.0$  km and  $z = 0.3$  km and forming a vertically-extending vortex just below  
209 the downward extruding cloud, outlined by the white isosurface of  $q_c$ , at the bottom of the  
210 supercell (Figure 4c). The extruding cloud resembles a funnel cloud that is often, but not always,  
211 a visual precursor of a tornado. As time goes on, the vortex intensifies and extends further both  
212 upward and downward, forming a long vortex from the ground all the way to the middle levels  
213 inside the supercell (Figure 4d). Also, the funnel cloud expands a bit. This cloudy vortex is long-  
214 lasting and evolving towards the end of the simulation. The vortex has a width of  $\sim 3$  km in the 1  
215 km simulation. The vortex in the 2 km case has a comparable size and that in the 500 m case is  
216 slightly thinner. These vortices are much wider than a typical tornado (hundreds of meters) but  
217 comparable to the widest “wedge” tornadoes, such as the 5-km wide tornado studied by Wurman  
218 et al. (2013). We refer to these cloudy vortices as “tornado-like vortices” hereafter, in analogy to  
219 the “tropical cyclone-like vortices” in 20-100 km global models (e.g., Zhao et al., 2012).

220 How did this funnel cloud form? Figure 5 shows the structure of the cloudy tornado-like  
221 vortex when it is fully developed (at the same moment as in Figure 4d). Near the ground (Figure  
222 5a), an area of moist air (water vapor  $q_v > 15 \text{ g}\cdot\text{kg}^{-1}$ ) forms in the forward flank of the supercell,  
223 which results from the evaporation of rainwater. This moist air can also be seen in a vertical  
224 cross-section cut through the cloudy vortex (Figure 5b). A region of saturated air forms near the  
225 ground in the  $y$  direction from 210 km to 215 km. This moist air then gets lifted into the rotating  
226 updraft, condenses water by adiabatic cooling, and forms the funnel cloud.

227

(a) Horizontal slice at  $z \approx 27$  m(b) Vertical slice at  $x = 221$  km

228

229 **Figure 5** Structure of cloudy vortex at 4350 s in the 1 km simulation. (a) horizontal cross-section  
 230 near the ground ( $z \sim 27$  m).  $q_v$  is plotted in color shading. Black contours represent  $q_l$  of 0.1, 1.0,  
 231 and  $5.0 \text{ g}\cdot\text{kg}^{-1}$ . White contours represent  $\zeta$  in the unit of  $0.001 \text{ s}^{-1}$ . (b) Vertical cross-section at  $x =$   
 232 221 km. Relative humidity (RH) is plotted in color shading. White contours represent  $\zeta$ , with  
 233 negative contours dashed and zero contour omitted. Wind vectors are plotted in black.

234

235 Next, we examine the formation of the tornado-like vortex through the vorticity equation.  
 236 The vertical vorticity equation in the height coordinates can be written as:

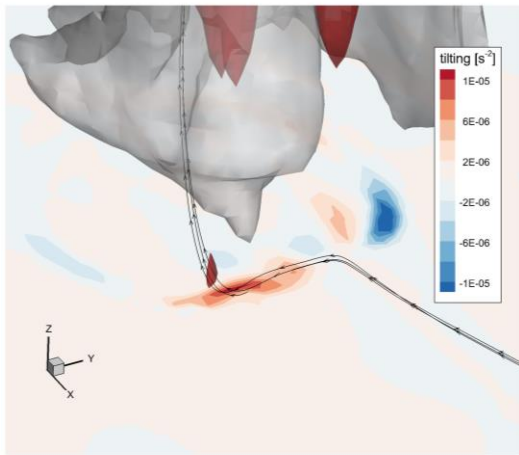
$$237 \quad \frac{\partial \zeta}{\partial t} = -\nabla \cdot \vec{v} \zeta - \zeta \left( \frac{\partial u}{\partial x} + \frac{\partial v}{\partial y} \right) + \left( \frac{\partial w}{\partial y} \frac{\partial u}{\partial z} + \frac{\partial w}{\partial x} \frac{\partial v}{\partial z} \right) + \left( \frac{\partial p}{\partial x} \frac{\partial \alpha}{\partial y} + \frac{\partial p}{\partial y} \frac{\partial \alpha}{\partial x} \right), \quad (3)$$

238 where  $p$  and  $\alpha$  are the pressure and specific density, respectively. Equation 3 describes that the  
 239 local tendency of  $\zeta$  is equal to, in order, advection, stretching, tilting, and baroclinicity.

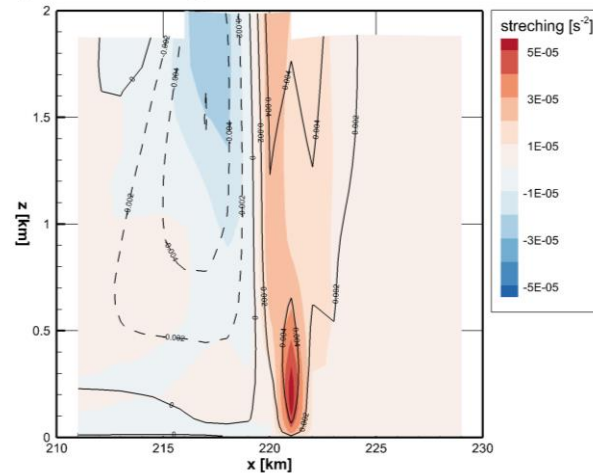
240 We compute each of the four terms within the 1-km simulation. It turns out that the tilting  
 241 and stretching terms play essential roles in forming the vortex, as has been found by numerous  
 242 studies on tornadogenesis (Davies-Jones, 2015; Markowski & Richardson, 2009; Orf et al., 2016;  
 243 Rotunno et al., 2017). Figure 6 shows the contribution from the tilting and stretching terms when  
 244 the vortex starts to develop (the same moment as in Figure 4c). Beneath the vortex, the tilting  
 245 term produces a positive  $\zeta$  near the ground (Figure 6a). This positive  $\zeta$  will get transported  
 246 upward by the updraft. At the same time, the stretching term has a local maximum right at the  
 247 developing tornado-like vortex near the ground (Figure 6b). The interpretation of Figure 6 is as  
 248 follows. First, the tilting term initiates a positive  $\zeta$  near the ground by redirecting the horizontal

249 vorticities (which results from the environmental vertical shear) through the horizontal gradient  
 250 of vertical velocity (which results from the main updraft developed locally in the supercell).  
 251 Second, the positive  $\zeta$  is brought upward by the updraft core and gets intensified by the  
 252 stretching term through convergence. Note that the stretching term cannot intensify or lessen  $\zeta$   
 253 without a preexisting  $\zeta$ . That is, the stretching term cannot create a positive/negative  $\zeta$  from zero  
 254 and only works to strengthen/weaken  $\zeta$ . The effects that the tilting and stretching terms have on  
 255 forming the tornado-like vortex are consistent with previous studies. It suggests that the  
 256 simulated vortices, even though coarsely resolved, are dynamically the same as real-world  
 257 tornadoes.  
 258

(a) Tilting term



(b) Stretching term



259  
 260 **Figure 6.** Two main contributors from the vorticity equation to the formation of the tornado-like  
 261 vortex when the vortex is about to develop (3750 s) in the 1 km case. (a) tilting term in a 3-  
 262 dimensional view. The solid red isosurface represents the tornado-like vortex (plotted by  $\zeta =$   
 263  $0.005 \text{ s}^{-1}$ ), while the transparent white isosurface represents the funnel cloud (plotted by  $q_c = 0.1$   
 264  $\text{g}\cdot\text{kg}^{-1}$ ). Color shading represents the contribution from the tilting term near the ground ( $z \sim 27$   
 265 m). Streamlines through the vortex are plotted. (b) stretching term in an  $xz$  cross-section cut  
 266 through the vortex ( $y = 209 \text{ km}$ ). Color shading represents the contribution from the stretching  
 267 term. Line contours show vertical vorticities, with negative contours dashed.

268

269 The baroclinicity and advection do not appear to play an important role in forming the  
 270 tornado-like vortex. The baroclinic term is at least one order of magnitude smaller than those

271 from the tilting and stretching terms near the vortex. The triviality of the baroclinic effect is  
272 discussed in both observational and theoretical papers (see section 3.2 in a review paper written  
273 by Davies-Jones, 2015). The advection term principally acts to move the vorticity maximum  
274 downstream.

## 275 **5 Conclusions and Discussion**

276 In the above, we present numerical simulations of a supercell storm at different  
277 resolutions on a full-size Earth using a newly developed global model. By utilizing a stretched  
278 global grid, the model can perform simulations on cloud-resolving scales using modest  
279 computational resources. The model is capable of producing a realistic supercell even at 4-km  
280 grid spacing. The storm morphology in all cases is consistent with observations and previous  
281 studies. It demonstrates a couple of interesting features of this simplified FV3-based model,  
282 including 1) a super-stretched global grid (up to a factor of 40) remains stable and accurate; 2)  
283 this setup could be a useful tool for process studies without the hassle of specifying lateral  
284 boundary conditions. It also shows the value of an FV3-based model for convective-storm  
285 simulation and prediction, which would apply equally well to regional contexts.

286 We found our simulated supercells also produced cloudy tornado-like vortices, which, to  
287 the best of our knowledge, have never before been simulated in the global modeling community.  
288 While wider than typical real-world tornadoes due to our grid cell sizes, the vortex is  
289 qualitatively similar to tornadoes: a funnel cloud with an intense vortex. It is found that, through  
290 analysis based on the vorticity equation, the tilting term initiates the vortices that are then  
291 intensified through stretching.

292 Previous modeling studies of tornadoes have used grid spacings of 50 m or smaller (Orf  
293 et al., 2017, and references therein). The capability of our model to produce tornado-like vortices  
294 at kilometer scales may reflect the strength of the D-grid staggering used in the FV3 dynamical  
295 core. On the D-grid, tangential winds are defined along grid boundaries, and so the circulation  
296 and thus by Stokes' Theorem cell-mean vorticity can be computed exactly. This may be the  
297 reason that our model can produce an intense vortex reminiscent of tornadoes even at kilometer  
298 scales, demonstrating the value of FV3's emphasis on vorticity dynamics.

299 Our model is capable of computing atmospheric flows and microphysics over a broad  
300 range of scales, ranging from tornado-like vortices to planetary waves. Our next step will be to  
301 take advantage of this capacity to study the cross-scale interactions involving supercells and

302 tornadoes. Gensini et al. (2019) studied the teleconnection between the U.S. tornadoes and  
303 planetary circulation features that were obtained from reanalysis data. The ability of our model to  
304 simulate multiple-scale atmospheric phenomena opens the opportunity to study such  
305 teleconnection dynamically, which in turn will lead to a better understanding of convective storm  
306 activity, both for storm prediction and projection under external forcing (Cheng et al. 2022).

307

### 308 **Acknowledgments**

309 The authors thank Chih-Chi Hu for valuable discussions. This study is supported under awards  
310 NA18OAR4320123, NA19OAR0220146, and NA19OAR0220147 from the National Oceanic  
311 and Atmospheric Administration (NOAA), U.S. Department of Commerce. This project was  
312 additionally funded under the NOAA Research Global-Nest initiative.

313

### 314 **Open Research**

315 Model used in this study is available at [https://github.com/NOAA-GFDL/SHIELD\\_build](https://github.com/NOAA-GFDL/SHIELD_build). Simulations  
316 presented in this study are available at <https://doi.org/10.5281/zenodo.8428465>.

317

### 318 **References**

319 Cheng, K.-Y., Harris, L., Bretherton, C., Merlis, T. M., Bolot, M., Zhou, L., et al. (2022). Impact  
320 of Warmer Sea Surface Temperature on the Global Pattern of Intense Convection: Insights From  
321 a Global Storm Resolving Model. *Geophysical Research Letters*, 49(16), e2022GL099796.

322 <https://doi.org/10.1029/2022GL099796>

323 Davies-Jones, R. (2015). A review of supercell and tornado dynamics. *Atmospheric Research*,  
324 158–159, 274–291. <https://doi.org/10.1016/j.atmosres.2014.04.007>

325 Gensini, V. A., Gold, D., Allen, J. T., & Barrett, B. S. (2019). Extended U.S. Tornado Outbreak  
326 During Late May 2019: A Forecast of Opportunity. *Geophysical Research Letters*, 46(16),  
327 10150–10158. <https://doi.org/10.1029/2019GL084470>

328 Harris, L., Zhou, L., Kaltenbaugh, A., Clark, S., Cheng, K.-Y., & Bretherton, C. (2023). A  
329 Global Survey of Rotating Convective Updrafts in the GFDL X-SHiELD 2021 Global Storm  
330 Resolving Model. *Journal of Geophysical Research: Atmospheres*, 128(10), e2022JD037823.  
331 <https://doi.org/10.1029/2022JD037823>

332 Harris, L. M., Lin, S.-J., & Tu, C. (2016). High-Resolution Climate Simulations Using GFDL  
333 HiRAM with a Stretched Global Grid. *Journal of Climate*, 29(11), 4293–4314.  
334 <https://doi.org/10.1175/JCLI-D-15-0389.1>

335 Harris, L., Chen, X., Putman, W., Zhou, L., & Chen, J.-H. (2021). A Scientific Description of the  
336 GFDL Finite-Volume Cubed-Sphere Dynamical Core. <https://doi.org/10.25923/6nhs-5897>

337 Jeevanjee, N., & Zhou, L. (2022). On the Resolution-Dependence of Anvil Cloud Fraction and  
338 Precipitation Efficiency in Radiative-Convective Equilibrium. *Journal of Advances in Modeling  
339 Earth Systems*, 14(3), e2021MS002759. <https://doi.org/10.1029/2021MS002759>

340 Judt, F., Klocke, D., Rios-Berrios, R., Vanniere, B., Ziemer, F., Auger, L., et al. (2021). Tropical  
341 Cyclones in Global Storm-Resolving Models. *Journal of the Meteorological Society of Japan*.  
342 Ser. II, 99(3), 579–602. <https://doi.org/10.2151/jmsj.2021-029>

343 Klemp, J. B., & Wilhelmson, R. B. (1978). The Simulation of Three-Dimensional Convective  
344 Storm Dynamics. *Journal of the Atmospheric Sciences*, 35(6), 1070–1096.  
345 [https://doi.org/10.1175/1520-0469\(1978\)035<1070:TSOTDC>2.0.CO;2](https://doi.org/10.1175/1520-0469(1978)035<1070:TSOTDC>2.0.CO;2)

- 346 Lin, S.-J. (1997). A finite-volume integration method for computing pressure gradient force in  
347 general vertical coordinates. *Quarterly Journal of the Royal Meteorological Society*, 123(542),  
348 1749–1762. <https://doi.org/10.1002/qj.49712354214>
- 349 Lin, S.-J. (2004). A “Vertically Lagrangian” Finite-Volume Dynamical Core for Global Models.  
350 *Monthly Weather Review*, 132(10), 2293–2307. [https://doi.org/10.1175/1520-](https://doi.org/10.1175/1520-0493(2004)132<2293:AVLFDC>2.0.CO;2)  
351 [0493\(2004\)132<2293:AVLFDC>2.0.CO;2](https://doi.org/10.1175/1520-0493(2004)132<2293:AVLFDC>2.0.CO;2)
- 352 Lin, S.-J., & Rood, R. B. (1997). An explicit flux-form semi-lagrangian shallow-water model on  
353 the sphere. *Quarterly Journal of the Royal Meteorological Society*, 123(544), 2477–2498.  
354 <https://doi.org/10.1002/qj.49712354416>
- 355 Markowski, P. M. (2002). Hook Echoes and Rear-F flank Downdrafts: A Review. *Monthly*  
356 *Weather Review*, 130(4), 852–876. [https://doi.org/10.1175/1520-](https://doi.org/10.1175/1520-0493(2002)130<0852:HEARFD>2.0.CO;2)  
357 [0493\(2002\)130<0852:HEARFD>2.0.CO;2](https://doi.org/10.1175/1520-0493(2002)130<0852:HEARFD>2.0.CO;2)
- 358 Markowski, P. M., & Richardson, Y. P. (2009). Tornadogenesis: Our current understanding,  
359 forecasting considerations, and questions to guide future research. *Atmospheric Research*, 93(1),  
360 3–10. <https://doi.org/10.1016/j.atmosres.2008.09.015>
- 361 Nesbitt, S. W., Salio, P. V., Ávila, E., Bitzer, P., Carey, L., Chandrasekar, V., et al. (2021). A  
362 Storm Safari in Subtropical South America: Proyecto RELAMPAGO. *Bulletin of the American*  
363 *Meteorological Society*, 102(8), E1621–E1644. <https://doi.org/10.1175/BAMS-D-20-0029.1>
- 364 Noda, A., & Niino, H. (2003). Critical grid size for simulating convective storms: A case study  
365 of the Del City supercell storm. *Geophysical Research Letters*, 30(16).  
366 <https://doi.org/10.1029/2003GL017498>

367 Nugent, J. M., Turbeville, S. M., Bretherton, C. S., Blossey, P. N., & Ackerman, T. P. (2022).  
368 Tropical Cirrus in Global Storm-Resolving Models: 1. Role of Deep Convection. *Earth and*  
369 *Space Science*, 9(2), e2021EA001965. <https://doi.org/10.1029/2021EA001965>

370 Orf, L., Wilhelmson, R., Lee, B., Finley, C., & Houston, A. (2016). Evolution of a Long-Track  
371 Violent Tornado within a Simulated Supercell. *Bulletin of the American Meteorological Society*,  
372 98(1), 45–68. <https://doi.org/10.1175/BAMS-D-15-00073.1>

373 Potvin, C. K., & Flora, M. L. (2015). Sensitivity of Idealized Supercell Simulations to Horizontal  
374 Grid Spacing: Implications for Warn-on-Forecast. *Monthly Weather Review*, 143(8), 2998–  
375 3024. <https://doi.org/10.1175/MWR-D-14-00416.1>

376 Putman, W. M., & Lin, S.-J. (2007). Finite-volume transport on various cubed-sphere grids.  
377 *Journal of Computational Physics*, 227(1), 55–78. <https://doi.org/10.1016/j.jcp.2007.07.022>

378 Rotunno, R., Markowski, P. M., & Bryan, G. H. (2017). “Near Ground” Vertical Vorticity in  
379 Supercell Thunderstorm Models. *Journal of the Atmospheric Sciences*, 74(6), 1757–1766.  
380 <https://doi.org/10.1175/JAS-D-16-0288.1>

381 Satoh, M., Stevens, B., Judt, F., Khairoutdinov, M., Lin, S.-J., Putman, W. M., & Düben, P.  
382 (2019). Global Cloud-Resolving Models. *Current Climate Change Reports*, 5(3), 172–184.  
383 <https://doi.org/10.1007/s40641-019-00131-0>

384 Schlesinger, R. E. (1978). A Three-Dimensional Numerical Model of an Isolated Thunderstorm:  
385 Part I. Comparative Experiments for Variable Ambient Wind Shear. *Journal of the Atmospheric*  
386 *Sciences*, 35(4), 690–713. [https://doi.org/10.1175/1520-](https://doi.org/10.1175/1520-0469(1978)035<0690:ATDNMO>2.0.CO;2)  
387 [0469\(1978\)035<0690:ATDNMO>2.0.CO;2](https://doi.org/10.1175/1520-0469(1978)035<0690:ATDNMO>2.0.CO;2)

388 Schmidt, F., 1977: Variable fine mesh in the spectral global models. *Beitr. Phys. Atmos.*, 50,  
389 211–217.

- 390 Stevens, B., & Bony, S. (2013). What Are Climate Models Missing? *Science*, 340(6136), 1053–  
391 1054. <https://doi.org/10.1126/science.1237554>
- 392 Stevens, B., Satoh, M., Auger, L., Biercamp, J., Bretherton, C. S., Chen, X., et al. (2019).  
393 DYAMOND: the DYNAMICS of the Atmospheric general circulation Modeled On Non-  
394 hydrostatic Domains. *Progress in Earth and Planetary Science*, 6(1), 61.  
395 <https://doi.org/10.1186/s40645-019-0304-z>
- 396 Toy, M. D. (2012). A Supercell Storm Simulation Using a Nonhydrostatic Cloud-Resolving  
397 Model Based on a Hybrid Isentropic-Sigma Vertical Coordinate. *Monthly Weather Review*,  
398 141(4), 1204–1215. <https://doi.org/10.1175/MWR-D-12-00215.1>
- 399 Ullrich, P. A., Jablonowski, C., Kent, J., Lauritzen, P. H., Nair, R., Reed, K. A., et al. (2017).  
400 DCMIP2016: a review of non-hydrostatic dynamical core design and intercomparison of  
401 participating models. *Geoscientific Model Development*, 10(12), 4477–4509.  
402 <https://doi.org/10.5194/gmd-10-4477-2017>
- 403 Wang, P. K., Cheng, K.-Y., Setvak, M., & Wang, C.-K. (2016). The origin of the gullwing-  
404 shaped cirrus above an Argentinian thunderstorm as seen in CALIPSO images. *Journal of*  
405 *Geophysical Research: Atmospheres*, 121(7), 2015JD024111.  
406 <https://doi.org/10.1002/2015JD024111>
- 407 Weisman, M. L., & Klemp, J. B. (1982). The Dependence of Numerically Simulated Convective  
408 Storms on Vertical Wind Shear and Buoyancy. *Monthly Weather Review*, 110(6), 504–520.  
409 [https://doi.org/10.1175/1520-0493\(1982\)110<0504:TDONSC>2.0.CO;2](https://doi.org/10.1175/1520-0493(1982)110<0504:TDONSC>2.0.CO;2)
- 410 Weisman, Morris L., & Rotunno, R. (2000). The Use of Vertical Wind Shear versus Helicity in  
411 Interpreting Supercell Dynamics. *Journal of the Atmospheric Sciences*, 57(9), 1452–1472.  
412 [https://doi.org/10.1175/1520-0469\(2000\)057<1452:TUOVWS>2.0.CO;2](https://doi.org/10.1175/1520-0469(2000)057<1452:TUOVWS>2.0.CO;2)

413 Wurman, J., Dowell, D., Richardson, Y., Markowski, P., Rasmussen, E., Burgess, D., et al.  
414 (2012). The Second Verification of the Origins of Rotation in Tornadoes Experiment:  
415 VORTEX2. *Bulletin of the American Meteorological Society*, 93(8), 1147–1170.  
416 <https://doi.org/10.1175/BAMS-D-11-00010.1>

417 Wurman, J., Kosiba, K., Robinson, P., & Marshall, T. (2013). The Role of Multiple-Vortex  
418 Tornado Structure in Causing Storm Researcher Fatalities. *Bulletin of the American*  
419 *Meteorological Society*, 95(1), 31–45. <https://doi.org/10.1175/BAMS-D-13-00221.1>

420 Zarzycki, C. M., Jablonowski, C., Kent, J., Lauritzen, P. H., Nair, R., Reed, K. A., et al. (2019).  
421 DCMIP2016: the splitting supercell test case. *Geoscientific Model Development*, 12(3), 879–  
422 892. <https://doi.org/10.5194/gmd-12-879-2019>

423 Zhao, M., Held, I. M., & Lin, S.-J. (2012). Some Counterintuitive Dependencies of Tropical  
424 Cyclone Frequency on Parameters in a GCM. *Journal of the Atmospheric Sciences*, 69(7), 2272–  
425 2283. <https://doi.org/10.1175/JAS-D-11-0238.1>

426 Zhou, L., Harris, L., Chen, J.-H., Gao, K., Guo, H., Xiang, B., et al. (2022). Improving Global  
427 Weather Prediction in GFDL SHiELD Through an Upgraded GFDL Cloud Microphysics  
428 Scheme. *Journal of Advances in Modeling Earth Systems*, 14(7), e2021MS002971.  
429 <https://doi.org/10.1029/2021MS002971>

430 Zavadoff, B. L., Gao, K., Lopez, H., Lee, S.-K., Kim, D., & Harris, L. M. (2023). Improved MJO  
431 Forecasts Using the Experimental Global-Nested GFDL SHiELD Model. *Geophysical Research*  
432 *Letters*, 50(6), e2022GL101622. <https://doi.org/10.1029/2022GL101622>

433